G55.0+0.3: A Highly Evolved Supernova Remnant

B. C. Matthews[1,2]

B. J. Wallace[3]

A. R. Taylor[1]

ABSTRACT

In order to determine the nature of an object identified as a potential supernova remnant (SNR) in a 327 MHz survey of the Galactic plane, continuum observations have been taken at 1420 MHz with resolution identical to that of the survey. Additionally, atomic hydrogen (HI) spectral line data have been taken in order to determine the distance to the object.

Multi-frequency analysis shows that a shell feature in the southern part of this object is non-thermal and confirms earlier studies that identified the northern portion as an HII region. The non-thermal nature of the shell and the absence of infrared flux density confirms the speculation of Taylor, Wallace, & Goss (1992) that this object, G55.0+0.3, is a SNR. From analysis of HI data, the SNR's estimated kinematic distance is 14 kpc, yielding a radius of approximately 70 pc, making it one of the largest known SNRs. The age estimate on the order of one million years exceeds the conventional limits on observable SNR lifetimes in the literature by a factor of five, implying that the radiative lifetimes of SNRs could be much longer than previously suggested.

There is also evidence that the remnant may be associated with the nearby pulsar J1932+2020. This proposed SNR/pulsar association is older than any previously documented by an order of magnitude. If valid, it suggests that searches for associations should not be restricted to the regions about young pulsars.

Subject headings: supernova remnants — ISM: individual (G55.0+0.3, G55.2+0.5, G55.6+0.7 — pulsars: individual (J1932+2020) — radio continuum: ISM

---

[1]Dept. Physics & Astronomy, University of Calgary, Calgary, AB, Canada, T2N 1N4

[2]Dept. Physics & Astronomy, McMaster University, Hamilton, ON, Canada, L8S 4M1

[3]Dominion Radio Astrophysical Observatory, P. O. Box 248, Penticton, BC, Canada, V2A 6K3

1. Introduction

There are 215 supernova remnants (SNRs) presently known in the Milky Way (Green 1996). Estimates of the fraction which could have been created by Type II supernovae (the core-collapse of massive stars) range from 75% (van den Bergh, McClure, & Evans 1987) to 85% (Tammann, Löffler, & Schröder 1994). Such collapses are also believed to form neutron stars, sometimes observable as pulsars. It has thus been expected that some large fraction of detectable SNRs should be associated with young pulsars. In fact, only a small number of observed associations exist; Caraveo (1995) summarizes 13 such associations, while Gaensler & Johnston (1995a) note that a total of 18 have been postulated.

Gaensler & Johnston (1995b) discuss reported SNR/pulsar associations and suggest from a statistical analysis that the expected number of observable associations is actually less than the reported number. The number of expected associations is strongly dependent on the observable lifetimes of SNRs. Currently, the oldest age estimates are on the order of 100,000 yr (e.g. CTB 80, Shull et al. 1989). Old radio remnants are likely to be physically large and have low surface brightnesses. Such objects may be difficult to separate from the Galactic background and are thus likely to be under-represented in current catalogues of SNRs.

Several very old SNRs may have already been detected, but lack of reliable distance estimates prevents the determination of either their physical sizes or their ages. Thus, our knowledge of SNR lifetimes is constrained more by theory than by observation. The detection of large and faint remnants can best be accomplished in high sensitivity, wide-field surveys of the Galactic plane. One such survey, conducted with the Westerbork Synthesis Radio Telescope (WSRT) at 327 MHz was sensitive to structures up to $45'$ in size (Taylor et al. 1996) and detected a number of new SNR candidates (Taylor et al. 1992). One of these candidates, G55.2+0.5, is a shell-like object coincident in position with a pulsar of spindown age 1.1×10^6 years, PSR J1932+2020. An association between the SNR and this pulsar, discovered in 1974 (Hulse & Taylor 1974, 1975), had been suggested previously by Crovisier (1974), but Reich et al. (1986) suggested instead that the emission in this region is produced by an H II region, not a SNR.

This paper's purpose is two-fold: to examine whether G55.2+0.5 is or contains a SNR; and to examine the possible association with PSR J1932+2020. To these ends, we have obtained new continuum observations of the region around G55.2+0.5 at 1420 and 408 MHz, as well as atomic hydrogen (H I) line observations. These observations are discussed in §2. In §3, we present the new data and compare them to data at a number of other wavelengths. The results of this analysis are discussed in §4 and summarized in §5.

2. The Observations

The observations for this investigation were carried out at the Dominion Radio Astrophysical Observatory (DRAO) in Penticton, British Columbia, Canada. The observatory is comprised of a synthesis telescope of seven antennae, each 9 m in diameter, and a 26 m single-dish antenna. The synthesis telescope is laid out on an east-west track. The second, third and fourth antennae are moveable, although they maintain a fixed spacing with respect to one another. These three antennae are moved daily over a period of twelve days so that the entire range of possible baselines from 12.9 m to 604.3 m are sampled at intervals of 4.3 m.

The DRAO synthesis telescope observes simulateously in continuum at 408 and 1420 MHz and on the spectral line of HI at 1420 MHz (λ21 cm). Short-spacings HI line data (to fill in missing baselines shorter than 12.9 m) are obtained with the 26 m dish. More information on the DRAO synthesis telescope can be found in papers by Roger et al. (1973) and Veidt et al. (1985).

The data were taken during the period from 6 August, 1992 to 23 September, 1992; one baseline was re-observed on 7 January, 1993. The field center is at right ascension $19^{\rm h}32^{\rm m}0^{\rm s}$ and declination $20^{\rm d}$ $6'$ $0''$ in J2000 coordinates. This position lies only 0.5° above the Galactic plane.

These data were among the first obtained after the DRAO upgrade from 4 to 7 antennae. The 1420 MHz continuum image contains an artifact at its centre which resulted from a correlator error that was present for a short period after the upgrade but was quickly fixed. Had the artifact been beam-shaped, we could have easily modeled and removed it. Despite initial appearances, however, it is not a signal which we would have expected from a point source at the centre (i.e. beam-shaped), and alternative methods were required to address the problem. To minimize the effects of the error, archival data from the same epoch were obtained from a high-declination field which did not have a source at the map centre. From these data, a model of the artifact containing minimal confusion with background sources was extracted. This artifact was corrected for the difference in north-south resolution of the interferometer and subtracted from the $u - v$ data of our field. A difference in the intensities of the two artifacts, the cause of which is not clear, required that only a fraction of the high-declination artifact be subtracted; the decision as to which fraction yielded the most satisfactory results was made by eye. The result of the subtraction was cosmetic improvement, but values of the affected pixels at the centre of the map remain unreliable. Fortunately, this region is not near the region of interest, which actually surrounds, but does not include, the centre of the map.

The continuum DRAO fields were self-calibrated and CLEANed using DRAO software. As with all interferometers, large spatial scale emission cannot be detected due to missing short-spacings. In the case of the DRAO interferometer, features larger than about one degree in size cannot be detected at 1420 MHz by the array (three degrees at 408 MHz). Single-dish data must be obtained to account for emission from large-scale sources. For this purpose, data from the 21 cm Effelsberg survey of Reich, Reich, & Fuerst (1990) and the 408 MHz all-sky survey of Haslam et al. (1983) were used.

The specifications for the DRAO continuum data are given in Table 1. Estimates of rms noise in the images were obtained by direct measurement of map fluctuations in a region of relatively low emission and are included in the table.

The DRAO synthesis telescope obtains HI line data at both left- and right-handed polarizations. The two polarizations were averaged together before mapping. The specifications of these data are summarized in Table 2. The level of emission in the HI data cube is sufficiently low that no self-calibration or CLEANing is possible. The continuum contribution to the HI cube was removed by subtracting a continuum map made from emission-free maps at either end of the HI data cube.

To obtain spectral information about the continuum emission, we have also used the 327 MHz data of Taylor et al. (1996) and the 2695 MHz data of Reich et al. (1984). In addition, we have obtained HiRes IRAS data (Aumann, Fowler, & Melnyk 1990; Cao et al. 1996; Fich & Terebey 1996) for this region at 60 and 100 microns. The details of these datasets are summarized in Table 3. This table contains the resolution of the data sets (in the case of the IRAS data, these are the HiRes values); the position angle (PA) east of north of the major axis of the beam; and the rms noise in the maps.

3. Results and Analysis

3.1. Radio Spectral Indices

The 327 and 1420 MHz data are presented in Figure 1. The images at these two frequencies have almost identical angular resolution. The 327 MHz image is purely interferometric and therefore contains no large scale smooth structures (i.e. greater than 45′ in angular size). The region of interest lies primarily to the north and south of the centre of the image and has three components – two bright compact regions of emission to the north and a partial shell structure to the south. Taylor et al. (1992) suggested these features may represent one object, a shell about 0.5° in diameter, designated by its central position of G55.2+0.5, as shown in Figure 1.

The centres of the northern structure and southern shell have coordinates G55.6+0.7 and G55.0+0.3 respectively. G55.6+0.7 contains two compact features superimposed on more extended emission. The position of the pulsar J1932+2020, marked by a cross on the figures, is within the east component of G55.6+0.7. The properties of the pulsar are summarized in Table 4 based on measurements by Lorimer et al. (1995). The uncertainties refer to the last significant digits in the measurements.

It is noteworthy that the coordinates G55.6+0.7 are those which were assigned to the radio source identified first as a potential SNR by Crovisier (1974) and later as a probable HII region by Reich et al. (1986). Aside from the features identified as components of a possible remnant by Taylor et al. (1992), a portion of the SNR HC 40 (G55.4−0.3) is visible as a saturated bright arc to the south-east in Figure 1. Other extended sources are visible as well; however, they are of smaller angular extent than G55.2+0.5 and HC 40.

Although they have poorer resolution than the 327 and 1420 MHz maps, maps of the region at 408 and 2695 MHz also reveal strong emission coincident with the features in the 327 and 1420 MHz maps. However, the individual components of G55.6+0.7 are not distinguishable at these frequencies.

The integrated flux densities of G55.6+0.7 and G55.0+0.3 were determined by summing the map intensities over the sources. The region of integration was set by enclosing each source in a polygon shape constructed on the image. The integrated flux density is the sum of the intensities within the polygon above a background plane, which is defined by fitting to the intensities at the vertices of the polygon. Before carrying out this procedure, the contribution from "point" (i.e. unresolved) sources within the polygon regions was removed. These sources are typically extragalactic and are removed so that they do not contribute to the measure of flux density from the extended, Galactic source.

Point source removal was performed on the 327 and 1420 MHz maps using Gaussian fitting. Gaussian fits could not be performed directly on the 408 and 2695 MHz images due to poor resolution. The flux densities obtained at 327 and 1420 MHz were used to extrapolate the 408 and 2695 MHz point source flux densities. These were subtracted from their integrated flux densities to remove the point source effects.

The presence of the pulsar added an additional difficulty to the integration of flux density over G55.6+0.7 and G55.2+0.5. The integrated flux density of pulsars may vary on long time scales, and there has been significant variation in the flux density measurements of this pulsar, with data from different epochs and with telescopes of different beamsizes. We have extrapolated all flux densities using the flux densities and spectral index of Lorimer et al. (1995).

At 327 MHz, the pulsar is visible in the image as an eastward extension of G55.6+0.7. The flux density at that point in the image is 40.5 mJy. The extrapolated flux density of the pulsar at 327 MHz from Lorimer et al. (1995) is 49.6 ± 12 mJy. For the purposes of removal of the pulsar's flux density, the most conservative estimate was taken; all the flux density observed at the pulsar's position was attributed to the pulsar itself. The contribution from the pulsar was far less significant at 1420 MHz, with an extrapolated flux density of 1.18 ± 0.4 mJy compared to an observed flux density of 211 mJy at the pulsar position. Thus, at this frequency, the pulsar's emission accounts for less than 1% of the observed flux density.

The polygons were created to match the regions of emission at 327 and 1420 MHz. Several polygons with approximately the same shape but different vertices were used to obtain independent estimates of the background, which is the greatest source of uncertainty in the determination of flux densities. The sums over polygons above background can be as little as 5% of the total flux densities. The backgrounds of each polygon were fit using a least-squares method to the edges of the region enclosed by the polygons and then subtracted. The resulting flux densities are listed in Table 5. The uncertainties are the standard deviations of the polygon means.

Using the integrated flux densities, the average spectral indices of the various features were determined. For each region, this was done by performing a weighted least-squares fit to the flux densities at each frequency. The resultant values for the radio spectral index are given in Table 6. The radio continuum spectra of G55.6+0.7 and G55.0+0.3 are plotted in Figure 2. The integrated spectrum of G55.0+0.3 indicates non-thermal emission since $\alpha = -0.53 \pm 0.26$ where $S_\nu \propto \nu^\alpha$. The average spectral index for known shell-type remnants is -0.47 ± 0.16 based on values from Green (1996). The northern source G55.6+0.7 could be indicative of thermal emission, since $\alpha = 0.01 \pm 0.10$.

The integrated flux densities provide a measure of the mean spectral index over each region. To look for a change in the spectral index within each region, we constructed spectral index maps from the 327 and 1420 MHz brightness temperature (T_b) images. Before constructing a spectral index map, the local background flux densities were removed by fitting independently to local regions around G55.6+0.7 and G55.0+0.3, and the pulsar's flux density was subtracted from the images.

Spectral index ratio maps are subject to large uncertainties in regions where the denominator image is close to zero. Thus, spectral indices were calculated only for those pixels with brightness temperatures greater than 12 K(T_b) above background at 327 MHz. This is the 3σ threshold, based on the measured noise in the 327 MHz map (see Table 3).

Uncertainties in the spectral index map from the noise present in the 327 and 1420 MHz maps are of order 0.1. After the removal of the pulsar, there was no significant variation in the spectral index of G55.6+0.7 and no evidence of non-thermal emission in any part of that region.

The spectral index map of G55.0+0.3 is shown in Figure 3. The quantity plotted is $2 - \alpha$. Significant, systematic variations in the brightness temperature spectral index appear within this structure. Those regions which appear black (≥ 2.2) are unambiguously non-thermal (the threshold value is 2.1). The white region of the map contains pixels for which the spectral index is not defined due to the low 327 MHz flux density.

Although most of the shell clearly shows non-thermal spectral indices, there is a large section in the southwest portion of the G55.0+0.3 which shows a flatter spectrum that could indicate either thermal or non-thermal emission. The presence of a thermal object in the foreground of the SNR could produce such a spectral index, or there may genuinely be a weaker shock at that position, decreasing the amount of non-thermal emission so the thermal background radiation is more prominent. The minimum value of the spectral index is $\alpha = -1.47$ at the southeast outer edge, while the maximum value is $\alpha = 0.34$ within the region to the southwest.

The spectral index analyses support both the suggestion of Taylor et al. (1992) that the region G55.2+0.5 contains a SNR (although it does not include the northern region) and the suggestion by Reich et al. (1986) that the northern collection of objects, G55.6+0.7, is an HII region.

3.2. IRAS Data

Figure 4 shows the HiRes 60 μm image of this region with 327 MHz continuum contours superimposed. No emission is present that is correlated to G55.0+0.3. However, there is heightened emission coincident with the northern source, G55.6+0.7.

Although a lack of 60 μm emission alone is insufficient to discriminate between objects of potentially similar morphology such as HII regions and SNRs, IRAS data in conjunction with radio data may be used to distinguish between objects of similar morphology in the two regimes (Arendt 1989; Saken, Fesen, & Shull 1992). Taylor et al. (1992) denoted values of the 60 μm to 327 MHz flux density ratios below 200 to be indicative of non-thermal sources. Table 6 summarizes the ratio for each region. These results support the conclusions of the radio analysis that G55.0+0.3 is an SNR and that G55.6+0.7 is an HII region.

Shull et al. (1989) note that some old remnants may be weak in radio, optical and X-ray emissions due to their low shock velocities, yet be extremely bright in the infrared. However, only one third of radio SNRs have been detected at infrared wavelengths, and faint radio remnants (e.g. G152.2−1.2, G291.9+5.5) are conventionally among those which have no detectable emission in the infrared (Arendt 1989). Thus, absence of IRAS emission might be expected for an evolved or faint SNR.

3.3. HI Line Data

The HI line data were used to search for evidence of atomic hydrogen associated with the radio continuum shell. The only obvious correlation was noted over nine velocity channels ranging from −39.6 to −52.8 km s^{-1}. Over this range, a void which matches the size and shape of the outer edge of the continuum emission shell is present. No evidence was found for high-velocity HI related to the SNR in the "empty" channels of the HI cube.

Figure 5 shows the velocity channels over which the void is present as well as additional channels on either end. For ease of presentation, a mean intensity bias has been subtracted from each channel. The correlation is strongest for the central channel, as would be expected for a symmetric expanding cavity and supports the notion that the void is related to the SNR. A continuum overlay on the central channel (−46.2 km s^{-1}) is shown in Figure 6.

The application of a flat Galactic rotation model with $R_\odot = 8.5$ kpc and $V_\odot = 220$ km s^{-1} yields a conversion of the LSR velocity to a kinematic distance of 14 kpc. The uncertainty associated with kinematic velocities due to the assumption of circular rotation of the Galaxy is on the order of 10% (Burton, 1988). The distance of G55.0+0.3 from the Galactic centre would therefore be $\sim$ 11 kpc, and its height above the Galactic plane would be $\sim$ 73 pc.

We superimposed a circle of radius 17.5′ to the shell of continuum emission, as shown in contour in Figure 6. At 14 kpc, this angular size implies a physical radius of $\sim$ 70 pc. This size is large, but not unprecedented. Table 7 summarizes the sizes of some of the largest SNRs for which distance estimates exist. The average physical radii (R_{avg}) are calculated for the lower distance limits (d_l) in the literature, which yield the lower limits on physical dimension.

4. Discussion

In summary, our analysis of the radio and 60 μm emission indicates that the half-shell of emission designated G55.0+0.3 is a supernova remnant. If it lies at a distance of 14 kpc as suggested by the association with the HI void at $v_{LSR} = -46.2$ km s^{-1}, its linear diameter is approximately 140 pc.

The 1 GHz surface brightness of the new remnant G55.0+0.3 is $(7.4 \pm 1.7) \times 10^{-23}$ W m^{-2} Hz^{-1} sr^{-1}, based on the angular size of 8.1×10^{-5} sr for the circular fit shown in Figure 6. Only one other SNR (G156.2+5.7) has a comparably low value of 6.2×10^{-23} W m^{-2} Hz^{-1} sr^{-1}. Based on the solid angle of the continuum shell alone of 2.9×10^{-5} sr, the surface brightness of the visible portion of the remnant is $(2.1 \pm 0.5) \times 10^{-22}$ W m^{-2} Hz^{-1} sr^{-1}. Thus, the remnant is among the faintest 10% of all remnants. This surface brightness, combined with its large angular and linear dimensions, suggests that it is highly evolved. In the next section, we attempt to place constraints on the age and evolutionary phase of G55.0+0.3.

4.1. Age via Evolutionary Models

As they expand, shell-type SNRs pass through four reasonably distinct phases as they merge into the interstellar medium (ISM). The four phase evolution, notwithstanding refinements, was first summarized by Woltjer (1972). The first phase, referred to by some as "free expansion", is characterized by a double-shock structure (McKee 1974). After the blast wave has swept through a significant amount of the ISM, the SNR enters the Sedov-Taylor phase, modeled as a point-blast into a uniform medium (Sedov 1959) and characterized by a $r^{2/5}$ expansion in time. This is followed by radiative expansion (when radiative cooling by metals causes a dense shell to form) and, finally, the merging of the remnant with the surrounding ISM.

The large physical size, low surface brightness and clumpy morphology of this remnant argue that it is in the late Sedov-Taylor or radiative phase of its expansion. After Shull et al. (1989), we use

$$R_s(t) = 31.5\ E_{51}^{0.2} n_0^{-0.2} t_5^{0.4} \quad \text{(pc)} \tag{1}$$

for the radius of a remnant in the Sedov-Taylor expansion stage, where E_{51} is the initial kinetic energy of the ejecta in units of 10^{51} erg, n_0 is the ambient interstellar hydrogen density in cm^{-3} (assumed to be constant), and t_5 is the SNR's age in units of 10^5 yr.

For times much greater than the onset of the pressure-driven snowplow, or radiative, phase, the model of Cioffi, McKee, & Bertschinger (1988) predicts the radius of the shell to be given by

$$R_s(t) \approx 27.9\ E_{51}^{0.221} n_0^{-0.257} \xi_m^{-0.0357} t_5^{0.3} \quad \text{(pc)} \tag{2}$$

which takes into account the the dynamics of the shell evolution and a radiative cooling function,

$$\Lambda(T) = (1.6 \times 10^{-19}) \xi_m T^{-0.5} \ \ (\text{erg cm}^{-3}\ \text{s}^{-1}) \tag{3}$$

where ξ_m is metallicity (equal to unity for solar abundances) and T is temperature. We have used $\xi_m = 1$ throughout our analysis. The form and constants of equations (1) and (2) are obviously dependent on assumptions of individual models. The above equations were generated for conditions of neglible presssure, spherical expansion, a homogeneous and uniform ISM and no thermal conduction (for more details, see Cioffi et al., 1988).

For G55.0+0.3, setting $R_s = 70$ pc in equations (1) and (2) yields expressions for the ages in the Sedov-Taylor and radiative phases to be:

$$t_5^{II} = 8\ E_{51}^{-0.5} n_0^{0.5} \quad (10^5\ \text{yr}) \tag{4}$$

and

$$t_5^{III} = 24\ E_{51}^{-0.737} n_0^{0.857} \xi_m^{0.119} \quad (10^5\ \text{yr}). \tag{5}$$

where superscripts II and III refer to the Sedov-Taylor and radiative phases, respectively.

The evolutionary model can be used to set reasonable limits on how old the remnant will be at the transition times between phases. These calculations can be used to establish, for a given distance, the evolutionary phase of the SNR.

The transition from Sedov-Taylor to radiative expansion occurs at

$$t_{rad} = (1.33 \times 10^4)\ E_{51}^{3/14} n_0^{-4/7} \xi_m^{-5/14} \quad \text{(yr)} \tag{6}$$

(Cioffi et al. 1988) where the radiative cooling function given by equation (3) has been used. Equating equations (4) and (6) yields the condition required for the remnant to be younger than t_{rad}. This condition can be written as

$$E_{51} \geq 300\ n_0^{1.5} \tag{7}$$

for density in units of cm^{-3}. If the remnant is in the Sedov-Taylor phase, then the inequality holds. Observations of extragalactic supernovae (SNe) give $E_{51} = 0.5$ to 2 (Wheeler

& Filippenko 1994; Arnett et al. 1989). The typical value for Type II SNe is 10^{51} erg (Chevalier 1977). We adopt an upper limit of 2 for E_{51} and thus obtain an upper limit on the ambient density, n_0, for the inequality to hold. Substitution into inequality (7) gives an upper limit on the density of 0.04 cm^{-3}. Unless $n_0 < 0.04$, the remnant is in the radiative phase.

Unfortunately, once a SNR enters Phase II, the information about the initial energy of the SN is not retained. However, estimation of the ambient density of the material with which the remnant is currently interacting can be made using the HI line data.

If the void in HI is taken to be the cavity in the ISM swept up by the remnant, we can use its diameter to estimate the pathlength through the HI which is occupied by the remnant, under the assumption that it has evolved in a roughly spherically symmetric fashion south of the blast position (i.e. it has formed a recognizable half-shell). The velocity width of the void therefore represents the velocity width of the HI evacuated by the remnant. In this case, the gas adjacent to the void within the same velocity interval is the unswept-up ISM occupying the same physical pathlength as the depth of the void. If the void is as deep as it is wide, this depth is 140 pc.

The density of the gas within this pathlength can be obtained from the column density over this velocity interval. It is obtained by integrating the brightness temperature (a sum of the velocity channels over which the void is evident) according to the expression:

$$n_0 = \frac{1.822 \times 10^{18}}{l} \Delta v \sum T_B(v) \tag{8}$$

where l is the length of the void along the line of sight in centimetres and Δv is the channel width in km s^{-1} (Rohlfs 1986). Figure 7 is a map of n_0 in the region of the remnant calculated from the nine velocity channels from -39.6 to -52.8 km s^{-1}. The values are of order unity everywhere adjacent to the shell. A large, low density region appears to the north. The low density of the ISM in this direction may explain the absence of a non-thermal shell there. Equations (4) and (5) both support faster expansions into regions of lower density, so there may be no evidence of a remnant remaining to the north.

The presence of turbulent motions in the ISM actually prevents the measurement of emission uniquely from regions as small as 140 pc. These turbulent motions will contribute emission from gas outside this pathlength interval. At the distance of the void of 14 kpc, the typical turbulent velocity of 8 km s^{-1} (Spitzer 1978) corresponds to a distance along the rotation curve of almost 2 kpc. Therefore, emission from gas displaced by up to ± 900 pc could spill over into the velocity interval of the void.

We have dealt with this excess of gas by presuming that the void is completely devoid of HI. Thus, the density estimate within the void is in effect a measure of the "background" contributions of the turbulent gas of the ISM. We also assume uniformity across our region of interest and thus simply subtract the "background" from the density estimates outside the void.

Taking into account the subtraction of the density estimate within, but near the edge of, the void ($\sim 1.6 \pm 0.1$ cm^{-3}) and the value just outside the void ($\sim 2.4 \pm 0.1$ cm^{-3}), this yields an ambient density estimate of 0.8 ± 0.2 cm^{-3} for the pre-swept-up gas, at least in the regions adjacent to the continuum half-shell. Over this half sphere, this density implies a swept-up mass of $\sim 10,000 M_\odot$ under the gross assumption (but one which we made above to estimate the contribution of turbulent motions in the ISM) that this cavity was swept clean by the expanding blast wave. This estimate of the swept-up mass is clearly an upper limit (see below).

In summary, the critical assumptions in this calculation are: that the cavity is as deep as it is wide (for the range of angles which the shell subtends); that the cavity is in effect devoid of HI; and that the contributions from the background ISM are uniform across and just outside the remnant. We have no way of estimating the density of the ISM in the past; thus, we also assume to first-order that the density of the ambient medium into which the remnant is currently expanding is the same as that of the material it has already swept up. Measurements of molecular material would be useful for obtaining further information about the region into which G55.0+0.3 is evolving.

A density of less than 0.04 cm^{-3} for the material *adjacent* to the shell is essentially ruled out by this analysis. Therefore, we conclude that the remnant is in the radiative phase, since the inequality of equation (7) does not hold. Additionally, unless our HI density estimate is incorrect by a factor greater than 1.5 orders of magnitude, the order of the resultant age will remain unchanged.

We have defined the time of the merger of the remnant with the ISM (dissipation) to be that at which the shock has slowed to 8 km s^{-1}, the speed of macroscopic turbulence in the ISM (Spitzer 1978). Differentiating equation (2) with respect to time and setting the result equal to the turbulence speed yields

$$t_{merger} = (2.9 \times 10^6)\ E_{51}^{0.316} n_0^{-0.367} m^{-1.43} \quad \text{(yr)} \tag{9}$$

where m is the local sound speed in units of 8 km s^{-1}.

If the density is indeed 0.8 ± 0.2 cm^{-3}, then the remnant has an age of $(1.9 \pm 0.4) \times 10^6$ yr, taking $E_{51} = 1$. The same model gives a merger time for the remnant of $3.1^{-0.2}_{+0.3} \times 10^6$ yr. A decrease in SN energy of $\sim 35\%$ produces radiative ages in excess of merger times while a corresponding increase inflates the merger time, but decreases the radiative age to just over one million years.

The ultimate ages obtained for the remnant depend on where one estimates the remnant boundary to be. However, a decrease in the physical size in excess of 20% is required to alter the radiative age to below one million years. This radius is well within the boundaries of the continuum shell.

Many assumptions were made to derive the density above, as we have already stated. Several of these have predictable consequences for the derived density. For instance, the assumption that the remnant has expanded into a region of uniform density is clearly a non-physical one, especially given its physical size. It is possible that the size of the void in the HI associated with the SNR owes its existence only partially or not at all to the actions of the SNR.

It is well-known that massive stars have powerful winds and are capable of sweeping out giant "bubbles" in the ISM over their lifetimes. Under such circumstances, the SNR formed by the final explosion of the star initially expands into a region of depleted ambient density. If this has indeed been the case for the remnant G55.0+0.3, then the age estimate calculated above is incomplete, since the remnant would have initially expanded into a region of circumstellar material of relatively low density. McKee, van Buren, & Lazareff (1984) conclude that a massive star which ends its life in a Type II SN will interact with circumstellar material to a radius of about 20 pc. Due to the low density in this regime, the total mass within this radius is comparable to the total mass of the stellar ejecta. Thus, the remnant would expand rapidly to this radius. The radius of the remnant G55.0+0.3 exceeds this value by greater than three times, implying that it should have evolved well past Phase I, even without taking into account its advanced morphology.

However, larger voids in the ISM can be created by clusters of massive stars during their lifetimes, or by the SNRs they spawn after death. If such a structure was created at the location of the SN which created G55.0+0.3, then the size of the currently visible void is the same as it was when the SN occurred. This scenario would invalidate all the previous dynamical calculations, since our estimate of the upper limit on the age assumes that the SNR has been interacting with an ISM of density 0.8 cm^{-3} for some large fraction of its lifetime. Such a pre-existing void could result in a remnant which is freely flowing to the north but has hit the edges to the south, forming the visible, non-thermal shell. Presuming that the remnant has just recently reached the southern boundary of any pre-existing void, we can assume that it has been expanding without hinderance for most of its lifetime. For an initial expansion velocity of 10^4 km s^{-1}, this yields an age of only about 7000 yr, which we consider to be an extreme lower limit.

The clumpy morphology and faintness of G55.0+0.3 leaves no doubt that the true age lies between the limits described above. Even though the upper limit is quite high, such ages cannot be dismissed out of hand as they are consistent with theoretical models. Expansion into a singular stellar wind bubble does not appear to occupy a significant fraction of the lifetime of a radiative remnant. The SNR is significantly younger only if it has expanded into a much larger cavity such as that which might be produced by a cluster of massive stars. The density estimate obtained from the HI is too high to suggest that an evacuated cavity exists now outside the continuum shell. Taking into account the likelihood that the remnant expanded into a pre-existing cavity for at least part of its lifetime, G55.0+0.3's radiative age of $\sim 10^6$ yr is taken to be an upper limit, although we reiterate that its size and morphology are indicative that it is likely in the radiative phase.

4.2. An SNR/Pulsar Association?

The proximity of PSR J1932+2020 to G55.0+0.3 begs the question as to whether or not these objects are related. Several factors argue in favour of an association.

Using the position of PSR J1932+2020 as given in Table 4 and a blast position of $19^{\rm h}32^{\rm m}4\overset{\rm s}{.}2$, $19^{\rm d}\ 58'\ 59\overset{''}{.}0$ (the centre of the circle in Figure 6), the pulsar's current position is $\sim 22'$ from the assumed position of the SN which created G55.0+0.3. This means the pulsar lies at an angular distance of only 1.3 times the radius of the remnant. To examine the possibility of a physical association further, we consider estimates of the distance and age of the pulsar.

From the dispersion measure, the distance of PSR J1932+2020 can be estimated to be approximately 9 kpc, with an uncertainty of 25% (Taylor & Cordes 1993). Measurements of HI absorption yield a lower limit of the turning point velocity to the v_{LSR} of the pulsar. Frail et al. (1991) measure an upper limit in HI absorption of -57 km s^{-1}. This is consistent with our limit of about -53 km s^{-1} for the HI void we associate with G55.0+0.3.

The characteristic age (i.e. spindown age $= P/2\dot{P}$) of pulsars provides a lower limit on their true age (although its value approaches the true value for large ages). The characteristic age of PSR J1932+2020 is 1.1×10^6 yr, based on data of Lorimer et al. (1995). This is consistent at the 2σ level with our estimate of the upper limit of the age of G55.0+0.3, $(1.9 \pm 0.4) \times 10^6$ yr.

Using the pulsar's spindown age of 1.1 million years, its average transverse velocity required to place it at the centre of the circular fit to G55.0+0.3 at birth is 80 km s^{-1}. The actual space velocity will be larger than this, depending on the inclination of the pulsar's velocity to the line of sight.

Proper motion measurements of Lyne, Anderson, & Salter (1982) have shown that pulsars are high-velocity objects. Using 71 objects, Cordes (1986) derived the mean transverse speed of pulsars to be 100 km s^{-1}, with a tail to the distribution extending to 300 km s^{-1}. Lyne and Lorimer (1994) have estimated the mean transverse pulsar birth speed to be 345 ± 70 km s^{-1} (rms 499 km s^{-1}) based on 29 pulsars younger than 3 Myr. The ten oldest pulsars give a mean velocity of 105 ± 25 km s^{-1}. The inferred velocity of ~ 80 km s^{-1} is thus in good agreement with typical old pulsar velocities.

The consistency of both the distance and age estimates of the pulsar and the remnant suggests that the two could be associated and could have been formed in the same SN event. If this is indeed the case, then the age of the SNR would be better established by that of the pulsar, since spindown estimates become more accurate as pulsars age.

Most of the SNR/pulsar associations which have been proposed are for the youngest known pulsars. Only one, CTB 80, has an age on the order of 10^5 yr, based on the spindown age of the pulsar B1951+32 (Shull et al. 1989). Most are $\sim 20,000$ yr old (Caraveo 1995). This is not surprising, since most have been found by focussed searches for associated SNR about young pulsars. This potential association of G55.0+0.3 and PSR J1932+2020 suggests that targeted searches should not be restricted by pulsars' characteristic ages.

From a statistical analysis, Shull et al. (1989) suggested that less than 1% of SNRs last for 10^6 yr, while fewer than 20% are still intact after 5×10^5 yr. If rare SNRs of ages on the order of a million years are visible, then the 20% which reach ages of 5×10^5 yr should also be detectable. These SNRs may simply have been too faint to be detected in previous radio surveys. Thus, the identification of such remnants is important for the statistics of both SNR properties and SNR/pulsar associations.

The age estimate of SNR G55.0+0.3 is well above the average age of the currently known SNR population of $\sim 60,000$ yr (Frail et al. 1994). At greater than one million years, the age of G55.0+0.3 is the oldest estimate for any radio detected SNR.

5. Conclusions

Based on the analysis of available radio and infrared data, we have determined that the composite object G55.2+0.5 contains one non-thermal source, designated G55.0+0.3. This radio half-shell has an average spectral index of -0.53 ± 0.26 and shows distinctly non-thermal emission across the majority of its surface. The radio spectrum of this object is consistent only with that of a shell-type SNR. The infrared/radio ratios for the region are also consistent with the values previously observed for shell-type SNRs. A spectral index of 0.01 ± 0.10 for G55.6+0.7 to the north and the heightened far-infrared emission are consistent with the results of Reich et al. (1986), who concluded that the object is an HII region.

HI line data show a void coincident with the continuum emission at a kinematic distance of 14 kpc. This implies a radius of 70 pc for the SNR at a height of ~ 73 pc above the Galactic plane. Analysis of the HI emission surrounding the void yields an ambient density of 0.8 ± 0.2 cm^{-3}. If the remnant is expanding into this material, it is in the radiative phase, and its age is estimated to be $(1.9 \pm 0.4) \times 10^6$ yr.

The assertion that the remnant is associated with the nearby pulsar, J1932+2020, is intriguing. The remnant and pulsar have comparable estimates of age and distance. If valid, the association would confirm the age of the SNR. At 14 kpc, a transverse velocity of 80 km s^{-1} corresponds to a proper motion of 1-2 mas per year. A proper motion measurement of the pulsar would aid in confirming or disproving the proposed association.

G55.0+0.3 is among the faintest SNRs known. This SNR could be just one member of a larger population of faint, old remnants that are not currently detectable at radio frequencies. If a significant fraction of SNR survive longer than 5×10^5 yr, further imaging of the Galactic plane with high surface brightness sensitivity and high angular resolution should reveal more old SNRs.

This research was supported by a grant to ART from the Natural Sciences and Engineering Research Council of Canada. The DRAO Synthesis Telescope is operated as a national facility by the National Research Council of Canada. BCM would like to thank ART and BJW for insightful feedback and strong encouragement throughout this project. We would also like to thank our referee for an insightful and thorough review.

REFERENCES

Arnett, W. D., Bahcall, R. P., Kirshner, R. P., & Woosley, S. E. 1989, ARA&A, 27,629

Arendt, R. G. 1989, ApJS, 70, 181

Aumann, H. H., Fowler, J. W., & Melnyk, M. 1990, AJ, 99, 1674

Burton, W. B. 1988, in Galactic and Extragalactic Radio Astronomy, ed. G. L. Vershuur & K. I. Kellermann (New York: Springer-Verlag)

Cao, Y., Prince, T. A., Tereby, S., & Beichman, C. A. 1996, PASP, 108 , 535

Caraveo, P. A. 1995, in The Lives of Neutron Stars, ed. M. A. Alpar et al. (Netherlands : Kluwer)

Chevalier, R. A., 1977, ARA&A, 15, 175

Cioffi, D. F., McKee, C. F., & Bertschinger, E. 1988, ApJ, 334, 252

Cordes, J. M. 1986, ApJ, 311, 183

Crovisier, J. 1974, A & A, 37, 189

Fich, M., & Terebey, S. 1996, ApJ, 472, 624

Frail, D. A., Cordes, J. M., Hankins, T. H., & Weisberg, J. M. 1991, ApJ, 382, 168

Frail, D. A., Goss, W. M. & Whiteoak, J. B. Z. 1994, ApJ, 437, 781

Fürst, E., Reich, W., & Seiradakis, J. H. 1993, A & A, 276, 470

Gaensler, B. M., & Johnston, S., 1995a, PASA, 12, 76

Gaensler, B. M., & Johnston, S., 1995b, MNRAS, 277, 1243

Graham, D. A., Haslam, C. G. T., Salter, C. J., & Wilson, W. E. 1982, A & A, 109, 145

Green, D. A., 1996, A Catalogue of Galactic Supernova Remnants (1996 August version), Mullard Radio Astronomy Observatory, Cambridge, United Kingdom (http://www.mrao.cam.ac.uk/ surveys/snrs/)

Haslam, C. G. T., Salter, C. J., Stoffel, H., & Wilson, W. E. 1983, A & AS, 47, 1

Hulse, R. A., & Taylor, J. H. 1974, ApJ, 191, L59

Hulse, R. A., & Taylor, J. H. 1975, ApJ, 201, L55

Leahy, D. A., & Roger, R. S. 1991, AJ, 101, 1033

Harrison, P. A. 1993, MNRAS, 263, 403

Lorimer, D. R., Yates, J. A., Lyne, A.G., & Gould, D. M. 1995, MNRAS, 273, 411

Lyne, A. G., Anderson, B., & Salter, C. J. 1982, MNRAS, 201, 503

Lyne, A. G., & Lorimer, D. R. 1994, Nature, 369, 127

McKee, C. F. 1974, ApJ, 188, 335

McKee, C. F., van Buren, D., & Lazareff, B. 1984, ApJ, 278, L115

Reich, W., & Braunsfurth, E. 1981, A & A, 99, 17

Reich, W., Reich, P., & Fuerst, E. 1990, A & AS, 83, 539

Reich, W., Fürst, E., Steffer, P., Reif. K., & Haslam, G. G. T. 1984, A & AS, 58, 197

Reich, W., Fürst, E., Reich. P., Sofue, Y., & Handa, T. 1986, A & A, 155, 185

Roger, R. S., Costain, C.H., Lacey, J. D., Landecker, T. L., & Bowers, F. K. 1973, Proc. IEEE, 61, 127

Rohlfs, K. 1986, Tools of Radio Astronomy (New York: Springer-Verlag)

Romney, J. D., Schilizzi, R. T., Fejes, I., & Spencer, R. E. 1987, ApJ, 321, 822

Routledge, D., Landecker, T. L., & Vaneldik, J. F. 1986, MNRAS, 221, 809

Saken, J. M., Fesen, R. A., & Shull, J. M. 1992, ApJS, 81, 715

Sedov, L. I. 1959, Similarity and Dimensional Methods in Mechancis, (New York: Academic Press)

Shull, J. M., Fesen, R. A., & Saken, J. M. 1989, ApJ, 346, 860

Spitzer, L. Jr. 1978, Physical Processes in the Interstellar Medium (New York : John Wiley and Sons)

Tammann, G. A., Löffler, W., & Schröder, A. 1994, ApJS, 92, 487

Taylor, A. R., Goss, W. M., Coleman, P. H., van Leeuwan, J., & Wallace, B. J. 1996, ApJS, 107, 239

Taylor, A. R., Wallace, B. J., & Goss, W. M. 1992, AJ, 103, 931

Taylor, J. H., & Cordes, J. M. 1993, ApJ, 411, 674

van den Bergh, S., McClure, R. D., & Evans, R. 1987, ApJ, 323, 44

Veidt, B. G., Landecker, T. L., Vaneldik, J. F., Dewdney, P. E., & Routledge, D. 1985, Radio Sci., 20, 1118

Wheeler, J. C., & Filippenko, A. V. 1994, in IAU Colloq. 145 Supernovae and Supernova Remnants, ed. R. McCray & Z. Wang (Cambridge: Cambridge Univ. Press)

Fig. 1.— These data are the 327 (left) and 1420 (right) MHz images. The images are 256 $\times$ 256 pixels with a grid scale of $30''$. The greyscale limits on the 327 MHz map are -30 (white) and 40 K(T_b) (black). The contour values are 10, 15, 20 and 30 K(T_b). The limits of the 1420 MHz map are 9.5 (white) and 13 K(T_b) (black), with contours ranging from 11 to 13 K(T_b) in increments of 0.4 K(T_b). The resolution of both maps is $1.0' \times 2.92'$.

Fig. 2.— The radio spectrum of G55.6+0.7 was generated with four frequencies (327, 408, 1420 and 2695 MHz) and is nearly flat. The spectrum for G55.0+0.3 (calculated without the flux density at 408 MHz due to confusion) is non-thermal. The flux densities at 327 MHz are underestimates due to the absence of short-spacings. The spectra were calculated after the effects of the pulsar and point sources were removed from each frequency. The error bars indicate 1σ standard deviations from the least squares fits. The slopes result in spectral indices of 0.01 ± 0.10 and -0.53 ± 0.26, respectively.

Fig. 3.— This spectral index map of G55.0+0.3 shows that not all of the shell revealed a non-thermal spectral index. Brightness temperature spectral indices less than 1.7 (or undefined on the exterior) appear white, while those greater than 2.2 (non-thermal) are black. Here, the spectral index is defined by $T_b \propto \nu^{2-\alpha}$, alpha given by $S_\nu \propto \nu^\alpha$. One large section in the southwest shows a spectral index that could be thermal. The circular region to the southeast of the SNR is most probably an HII region.

Fig. 4.— This figure compares infrared to radio emission over the same region as the maps of Figure 1. The greyscale shows the distribution of infrared emission at 60 μm. Black indicates emission greater than 150 MJy sr^{-1}, while white indicates emission below zero. The overlaid contours at 327 MHz have values of 10, 15, 20, 25, 30, 35, 40 and 45 K(T_b). Note that there is a source of IRAS emission coincident with the radio source G55.6+0.7; however, the southern shell has no such counterpart, containing only a semi-compact infrared source near its southeast corner. Some infrared point sources were subtracted from the map for the determination of flux densities using polygons. The black cross marks the position of the pulsar J1932+2020.

Fig. 5.— HI Velocity Channels: -34.6 to -56.1 km s^{-1}. These bias-subtracted maps have limits of -15 (black) and 20 (white) K(T_b). A single black contour is included at -5 K(T_b). A 327 MHz continuum contour map is shown in the centre with contours of 10, 15, 20 and 25 K(T_b). The continuum map is included separately as its contours tend to obscure the HI below. Bias-subtraction was performed solely to allow the presentation of all maps on the same scale. A larger image of the central channel is shown in Figure 6. A void (partial or total) coincident with the continuum shell can be seen from velocities of -39.6 to -52.8 km s^{-1}. Several channels, where no structures correlated to the continuum shell were seen, are

shown on either side of these.

Fig. 6.— Central HI map for $v_{LSR} = -46.2$ km s^{-1}. The shell at 327 MHz in white contours (5, 10, 15 and 20 K(T_b)) is matched well by the HI greyscale void at -46.2 km s^{-1}. Many of the variations in the continuum are echoed in the void, especially to the southeast. The greyscale limits for the HI are 20 (white) and -15 K(T_b) (black). The single black contour in HI is placed at 0 K(T_b). The map has been bias-subtracted. The $35'$ circle indicates an approximate diameter for the remnant.

Fig. 7.— This density map was calculated under the assumptions of spherical expansion of the remnant. The map has a grid spacing of $30''$. The greyscale limits are 0 (black) to 3 cm^{-3} (white), while the contours are 1.4, 1.6, 1.8 and 2 cm^{-3} respectively. A single white contour at 10 K(T_b) of the 327 MHz continuum has been added to indicate the location of the shell. The estimated uncertainty on each density measurement is 6%.

Table 1: **DRAO Synthesis Data Specifications**

	408 MHz (λ74 cm)	1420 MHz (λ21 cm)
central frequency	408 MHz	1420.406 MHz
polarization	left circular	right circular
continuum bandwidth	4 MHz	30 MHz
system temperatures	150 K	65 K
field size (to 20% response)	8.1°	2.6°
synthesized beam (EW × NS)	$3.4' \times 9.8'$	$1.0' \times 2.92'$
measured rms noise (T_b)	854 mK	40 mK

Table 2: **Specifications of Synthesis HI Spectral Line Data**

polarization	left and right circular
bandwidth	1 MHz
field size (to 20% response)	2.6°
synthesized beam (EW x NS)	$1.74' \times 5.10'$
rms noise in the map centre/channel (T_b)	1.17 K
central velocity	0 km s^{-1}
total 128 channel span	211 km s^{-1}
channel separation	$\sim$ 1.65 km s^{-1}
channel width	$\sim$ 2.6 km s^{-1}

Table 3: **Specifications of Images at Alternate Wavelengths**

λ/ν	Resolution	PA (N of E)	rms noise
60 μm	$1.67' \times 1'$	340°	21%[a]
100 μm	$2.42' \times 1.92'$	335°	32%[a]
11 cm / 2695 MHz	$4.27' \times 4.27'$	—	24 mK(T_b)
92 cm / 327 MHz	$1' \times 2.92'$	90°	4 K(T_b)

[a]Infrared Processing and Analysis Center estimated uncertainty in spatially integrated flux densities over a source (Fich & Terebey 1996)

Table 4: **Established Parameters of PSR J1932+2020**

		1σ
RA	$19^{\rm h}32^{\rm m}8\overset{\rm s}{.}30$	3
Dec	$20^{\rm d}\ 20'\ 46\overset{''}{.}30$	6
Period, P	0.268216854361 s	3
$\dot{P}(\times 10^{-15})$	4.21630	18
dispersion measure	211.007 $\rm cm^{-3}pc$	17

Table 5: **Integrated Flux Densities over a Series of Polygons**

Region	# polygons averaged	S_{2695} (Jy)	S_{1420} (Jy)	S_{408} (Jy)	S_{327} (Jy)
east G55.6+0.7	13	—	0.088 ± 0.012	—	0.057 ± 0.013
west G55.6+0.7	11	—	0.037 ± 0.005	—	0.038 ± 0.008
G55.6+0.7	7	1.0 ± 0.1	1.3 ± 0.1	1.17 ± 0.14	0.91 ± 0.13
G55.0+0.3	14	0.27 ± 0.05	0.64 ± 0.11	0.25 ± 0.12	0.98 ± 0.15
G55.2+0.5	12	1.7 ± 0.1	2.9 ± 0.3	2.4 ± 0.3	2.75 ± 0.31

Table 6: **Radio Spectral Indices and Infrared/Radio Ratios**

	east G55.6+0.7	west G55.6+0.7	G55.6+0.7	G55.0+0.3	G55.2+0.5
α	0.30 ± 0.13	-0.01 ± 0.10	0.01 ± 0.10	-0.53 ± 0.26	-0.21 ± 0.19
$S_{60\mu m}/S_{327{\rm MHz}}$	1063 ± 361	237 ± 155	503 ± 121	155 ± 53	275 ± 60

Table 7: **SNRs of Large Radii**

SNR	Angular Size	d_l (kpc)	R_{avg} (pc)	Reference
G160.9+2.6 (HB 9)	$140' \times 120'$	<4	<150	Leahy & Roger (1991)
G39.7−2.0	$120' \times 60'$	4.5	120	Romney et al. (1987)
G166.2+2.5 (OA 184)	$90' \times 70'$	8	90	Routledge et al. (1986)
G116.5+1.1	$80' \times 60'$	3.6	70	Reich et al. (1981)
G114.3+0.3	$90' \times 55'$	3	60	Fürst et al. (1993)
G205.5+0.5	$220' \times 220'$	0.8	50	Graham et al. (1982)

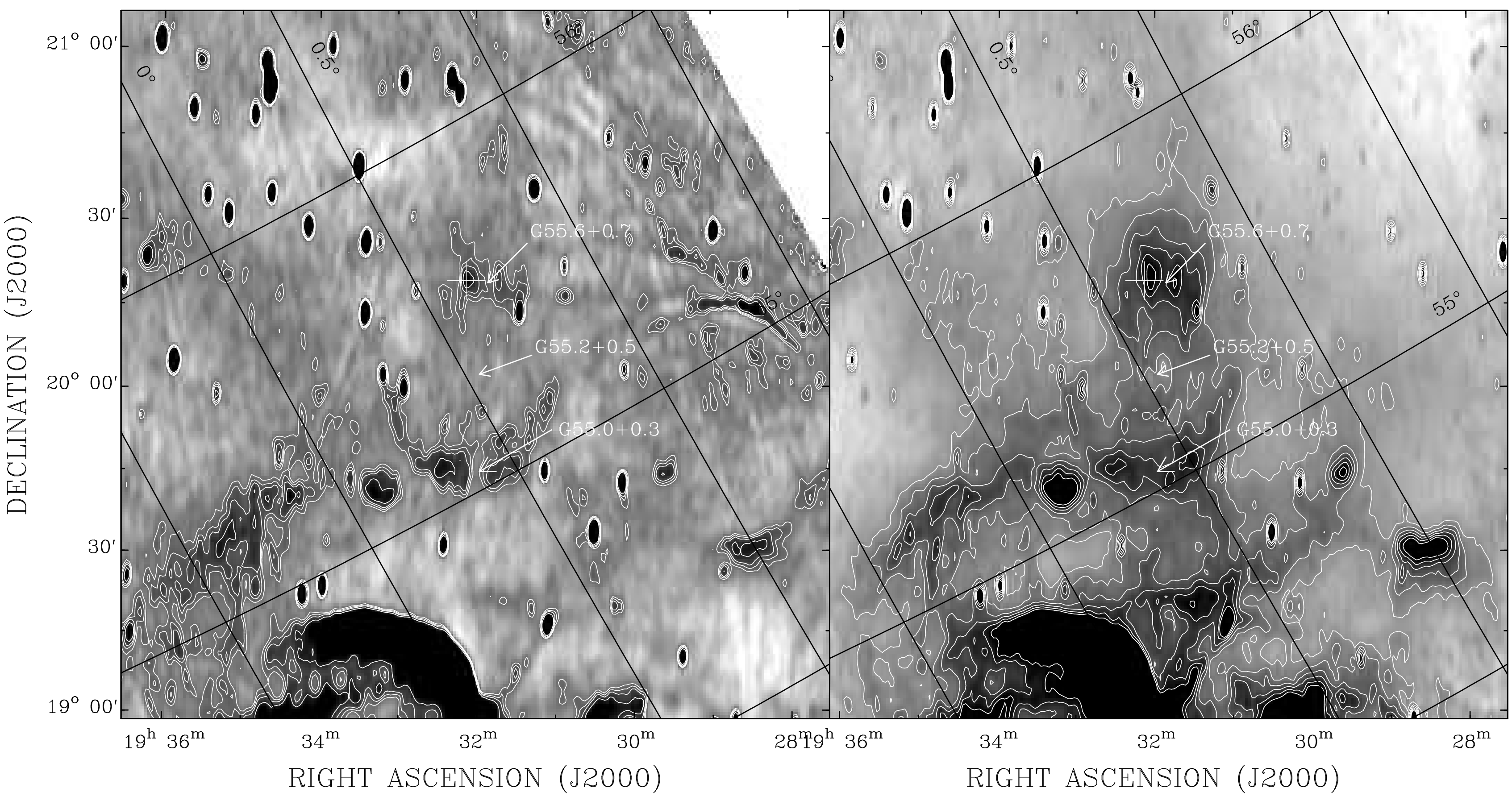
21° 00′
30′
20° 00′
30′
19° 00′
DECLINATION (J2000)
0°
0.5°
56°
55°
G55.6+0.7
G55.2+0.5
G55.0+0.3
19h 36m
34m
32m
30m
28m
RIGHT ASCENSION (J2000)
19h 36m
34m
32m
30m
28m
RIGHT ASCENSION (J2000)

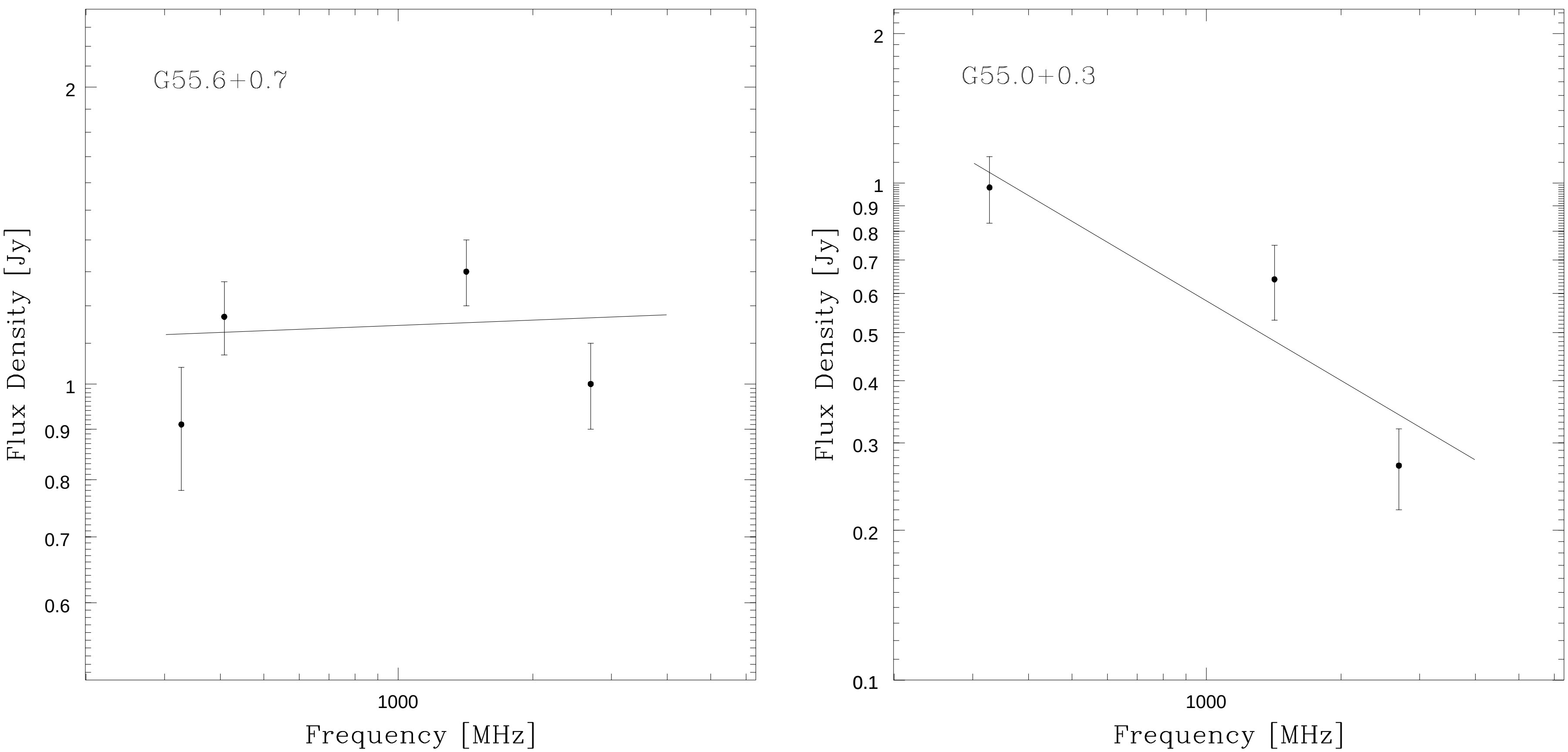
G55.6+0.7
Flux Density [Jy]
2
1
0.9
0.8
0.7
0.6
1000
Frequency [MHz]
G55.0+0.3
Flux Density [Jy]
2
1
0.9
0.8
0.7
0.6
0.5
0.4
0.3
0.2
0.1
1000
Frequency [MHz]

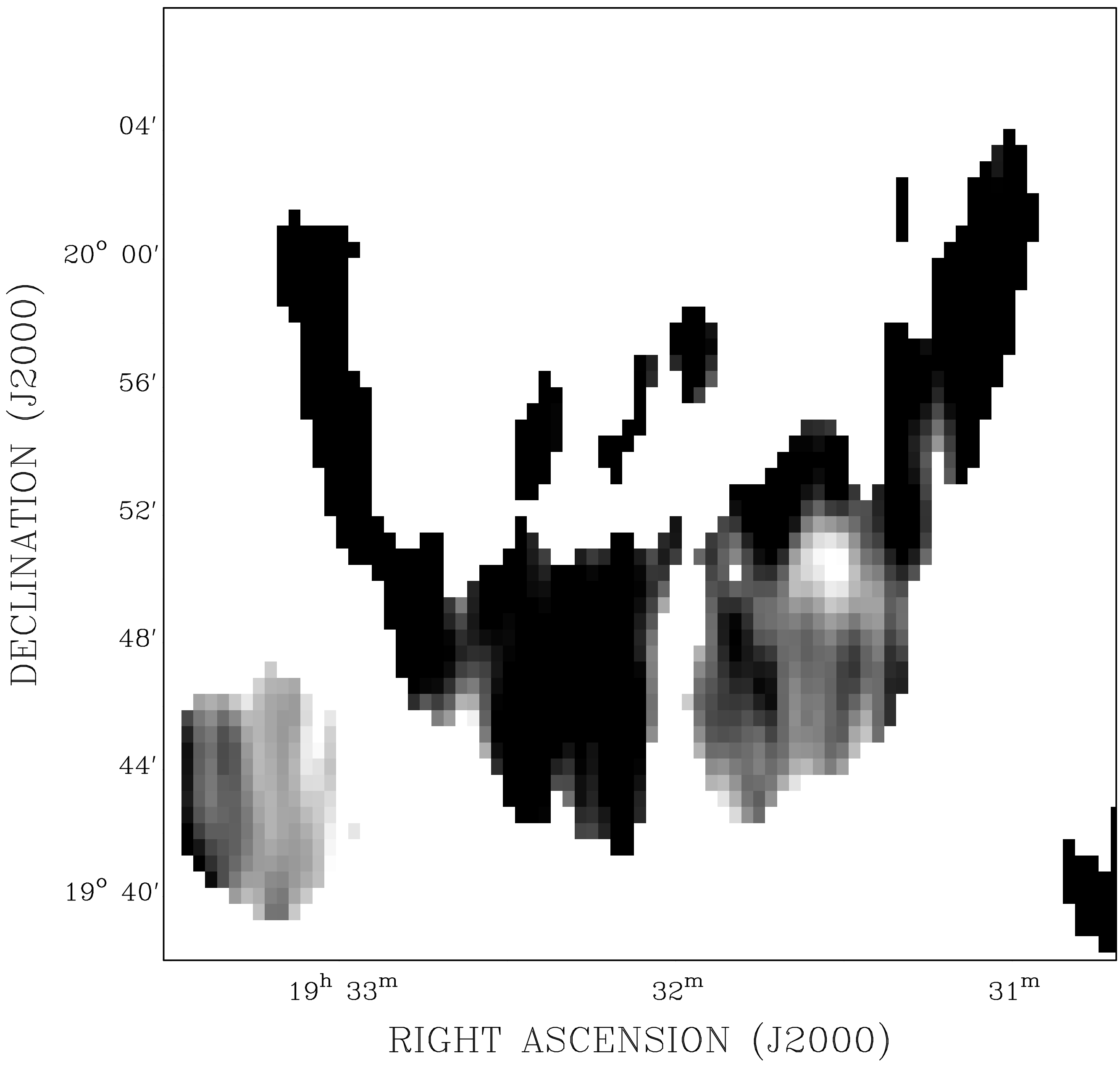

04′
20° 00′
56′
52′
48′
44′
19° 40′
DECLINATION (J2000)
19h 33m
32m
31m
RIGHT ASCENSION (J2000)

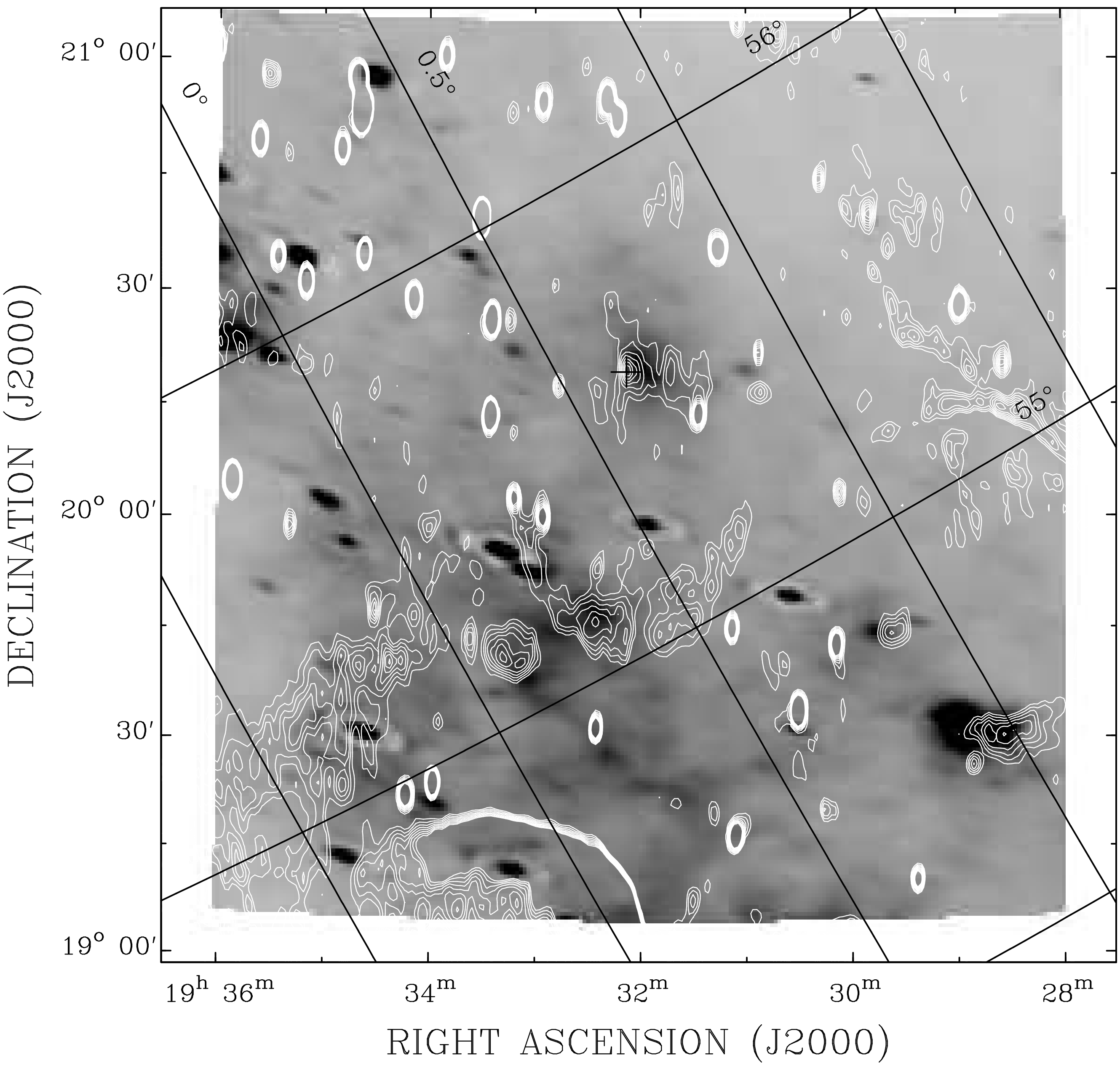

DECLINATION (J2000)
21° 00′
30′
20° 00′
30′
19° 00′
RIGHT ASCENSION (J2000)
19h 36m
34m
32m
30m
28m
0°
0.5°
56°
55°

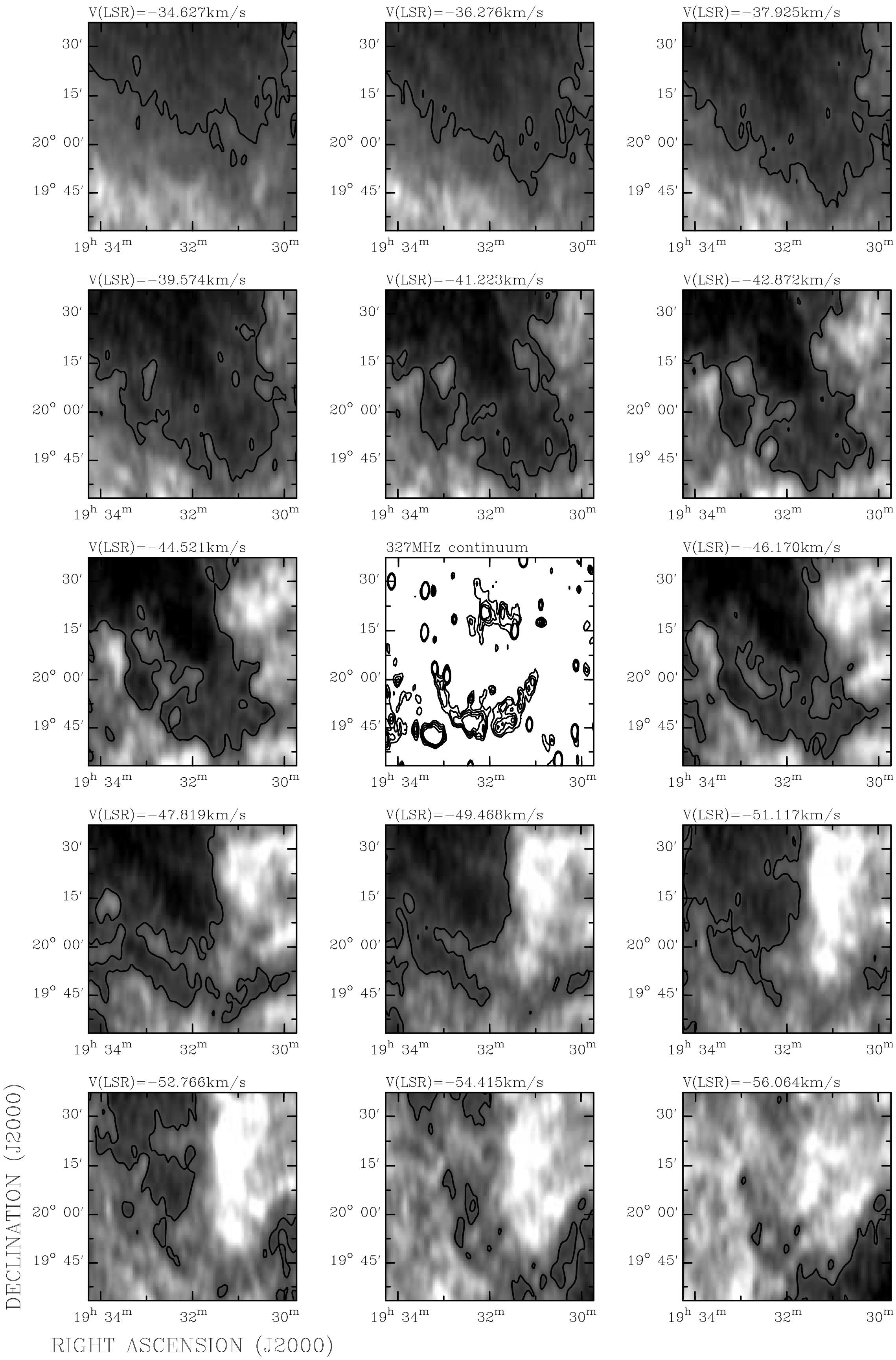
V(LSR)=−34.627km/s
V(LSR)=−36.276km/s
V(LSR)=−37.925km/s
V(LSR)=−39.574km/s
V(LSR)=−41.223km/s
V(LSR)=−42.872km/s
V(LSR)=−44.521km/s
327MHz continuum
V(LSR)=−46.170km/s
V(LSR)=−47.819km/s
V(LSR)=−49.468km/s
V(LSR)=−51.117km/s
V(LSR)=−52.766km/s
V(LSR)=−54.415km/s
V(LSR)=−56.064km/s
30′
15′
20° 00′
19° 45′
19h 34m
32m
30m
DECLINATION (J2000)
RIGHT ASCENSION (J2000)

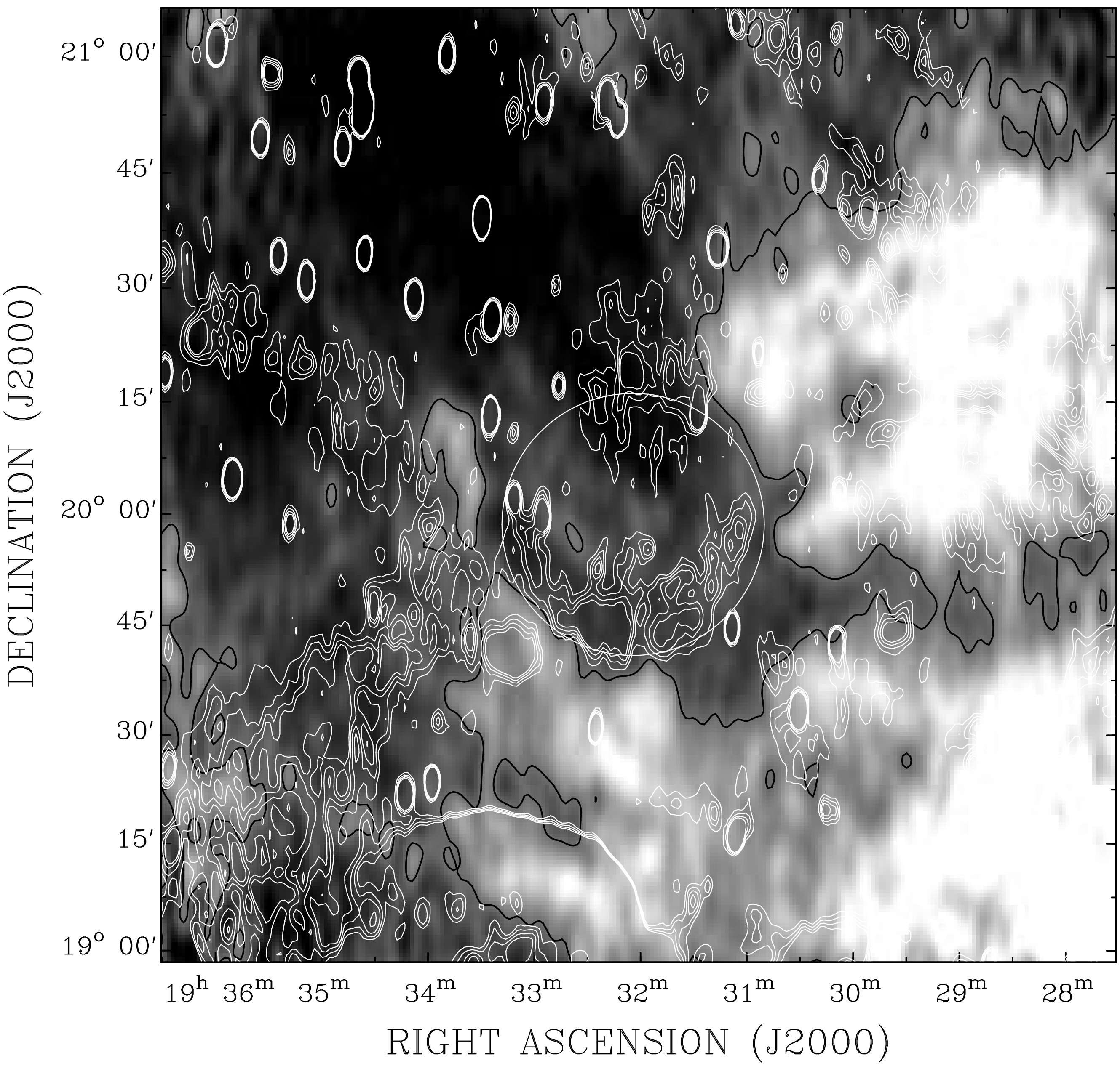
21° 00′
45′
30′
15′
20° 00′
45′
30′
15′
19° 00′
DECLINATION (J2000)
19h 36m
35m
34m
33m
32m
31m
30m
29m
28m
RIGHT ASCENSION (J2000)

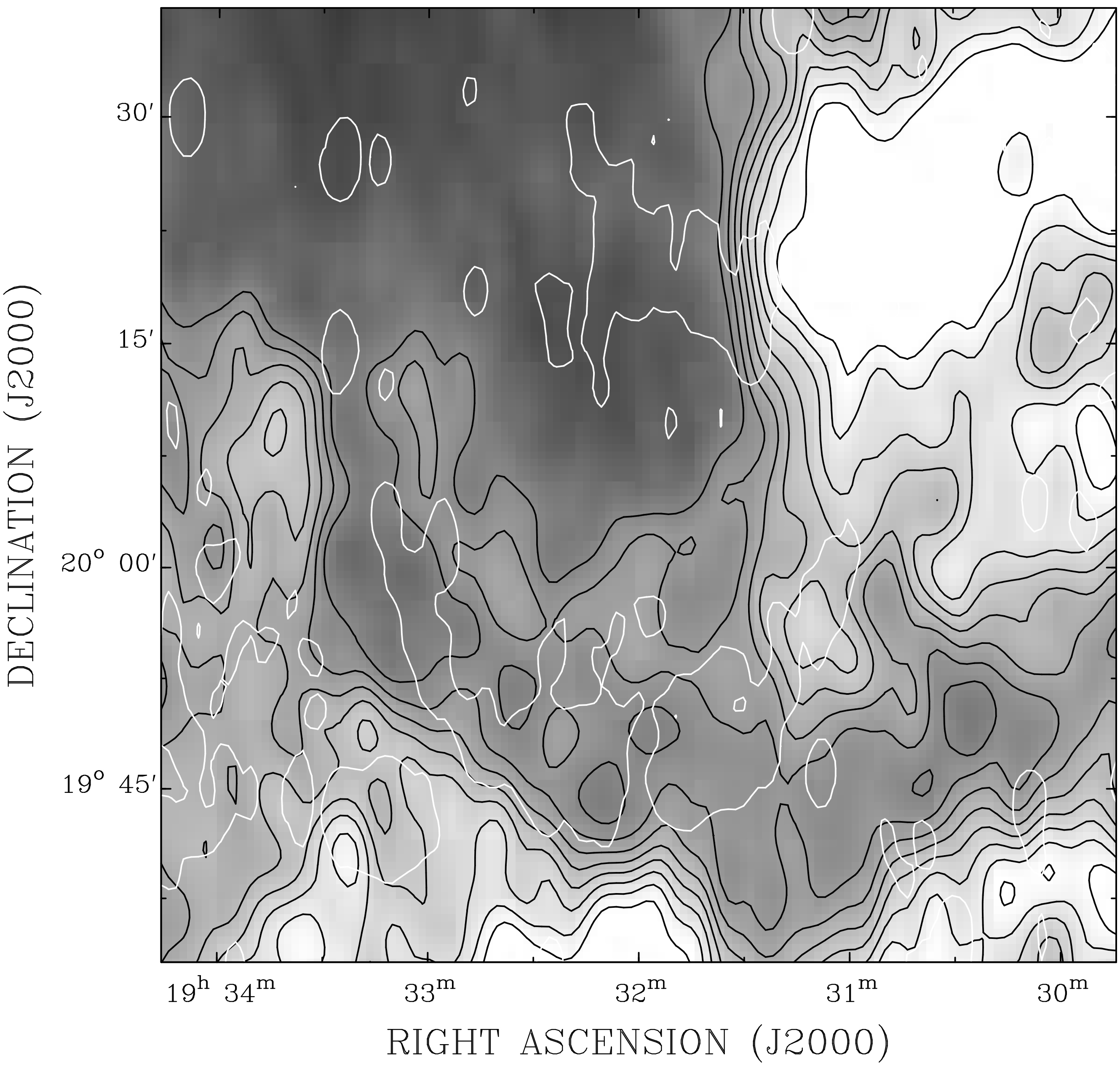

DECLINATION (J2000)
30′
15′
20° 00′
19° 45′
19h 34m
33m
32m
31m
30m
RIGHT ASCENSION (J2000)